

PAPER • OPEN ACCESS

Acoustic radiation from random waves on plates




To cite this article: Neezar M Mohammed *et al* 2022 *J. Phys. A: Math. Theor.* **55** 394004

View the [article online](#) for updates and enhancements.

You may also like

- [Acoustic radiation force on a rigid cylinder near rigid corner boundaries exerted by a Gaussian beam field](#)
Qin Chang, , Yuchen Zang et al.
- [Acoustic radiation pressure in laterally unconfined plane wave beams](#)
John H Cantrell
- [Quantitative measurement of acoustic radiation force on a thin catheter for use in endovascular therapy](#)
Takashi Mochizuki, Nobuhiro Tsurui, Naoto Hosaka et al.

Acoustic radiation from random waves on plates

Neekar M Mohammed^{1,2} , Stephen C Creagh¹ 
and Gregor Tanner^{1,*} 

¹ School of Mathematical Sciences, University of Nottingham, United Kingdom

² Department of Mathematics, College of Science, University of Sulaimani, Sulaymaniyah, Kurdistan Region, Iraq

E-mail: gregor.tanner@nottingham.ac.uk

Received 10 February 2022, revised 2 August 2022

Accepted for publication 23 August 2022

Published 8 September 2022



Abstract

Controlling and simulating the sound radiating from complex structures is of importance in many engineering applications. We calculate the radiated acoustic power from plates with diffuse bending vibrations. We characterise the diffuse field by a two-point correlation function (CF) of normal velocities. Given the relation between field–field CFs and ray-dynamical phase space densities, the approach taken here offers a basis for coupling structure borne ray-tracing techniques with acoustic radiation. At the same time, it caters for stochastic, noisy driving of such systems. The results for the radiation efficiency of a plate are presented in an asymptotic form analogous to the Weyl formula for the density of states. Leading contributions from the plate interior and its boundary are derived, with corner corrections also being given for particular boundary conditions and right-angled corners. A notable feature of this analysis is that the bulk contribution vanishes below a critical frequency, and the asymptotic estimate of radiated power then leads with a boundary contribution. This is shown to agree well with a more traditional calculation based on modal analysis in the special case of a rectangular plate.

Keywords: acoustic radiation, radiation efficiency, diffuse field excitation, random waves, correlation function

(Some figures may appear in colour only in the online journal)

* Author to whom any correspondence should be addressed.



Original content from this work may be used under the terms of the [Creative Commons Attribution 4.0 licence](https://creativecommons.org/licenses/by/4.0/). Any further distribution of this work must maintain attribution to the author(s) and the title of the work, journal citation and DOI.

1. Introduction

This paper treats the radiation of sound from plates excited by random vibrational wave fields. Detailed results are given for the case of vibrational fields that are isotropically and homogeneously diffuse. The approach taken can also be applied when the vibrational field is non-uniform or non-diffuse as obtained numerically by structure borne ray-tracing simulations such as the dynamical energy analysis [1]. We concentrate on radiation *efficiency* as a measure of how successfully the vibrating structure couples acoustically to the surrounding air. While this quantity can be defined for arbitrary structures, the standard definitions often assume single-frequency excitation and planar structures of arbitrary shape [2], which is the case treated here.

A particularly notable result is that, below a critical frequency, where the wavelength of vibrational waves is shorter than the wavelength of sound in air, the radiated power can be approximated simply as a boundary integral, which depends at leading order on the boundary conditions imposed. Here the radiated acoustic field from the interior of the plate is evanescent and does not carry power to the farfield: any radiated power is instead generated by the diffractive, sharp cut-off at the plate's edge. We express this radiated power analytically as a boundary integral that explicitly incorporates boundary conditions on the plate. This asymptotic result is part of a series for the radiated power that is analogous to the Weyl formula for the density of states of a cavity problem [3–5]. Above the critical frequency the leading term in this series is proportional to the area of the plate and the boundary contribution represents a small correction to this, which we do not compute explicitly. Below the critical frequency, however, the term proportional to area in fact vanishes, and then the boundary correction is the leading term.

Our approach to calculating (leading) contributions to this series is analogous to historical approaches to derivation of the Weyl series [3–5]. The bulk term proportional to the area is obtained by characterising the correlation function (CF) in the plate's interior using a free-space model that neglects the effect of the boundary itself. The boundary contribution is obtained by adding corrections using the method of images, and approximating the boundary locally in the contributing layer by a straight line. One can in principle extend this development to higher order terms in the series controlled by boundary curvature and corners. We do not perform this analysis in detail, but do provide such a correction in the special case of right-angled corners below the critical frequency (which turns out to vanish, like the bulk term).

Characterising and simulating sound radiation from structures has a long history. Analytical expressions for sound radiation from finite planar surfaces have, for example, been provided by Junger and Feit [6], Fahy [2] and Cremer *et al* [7] for the farfield and by Cremer *et al* [7] for the nearfield. Studying sound radiation from vibrating plate-like structures serves as a first step in understanding and manipulating sound radiated from more complex structures.

Earlier studies of sound radiation efficiency have dealt mostly with simple rectangular plates or strips. Maidanik [8] suggested a statistical approach estimating the structural vibration of ribbed panels in response to acoustic excitation and studied the effects of different boundary conditions theoretically and experimentally. Wallace [9, 10] proposed numerical integration methods for finding approximate solutions for the single-mode radiation efficiency of a baffled beam and rectangular plates. In terms of the acoustic power radiated into the far-field, the radiation resistance corresponding to individual modes is computed. Gomperts [11] tested the acoustic radiation efficiency of a baffled rectangular plate and showed that implementation of edge restrictions may not always increase radiated acoustic waves into the far-field. He additionally found that the radiation efficiencies of two-dimensional vibrating structures vary

rather impressively from those for one-dimensional vibrating structures. By using a Fourier transform method in wavenumber space, Heckl [12] studied the radiation patterns of planar sources. A series of asymptotic formulas were published by Loppington *et al* [13] to estimate the radiation efficiency of different plates, in particular for large structural wavenumbers and near-critical frequencies. In order to analyse the sound power originating from planar sources, Williams [14] suggested an expansion in the powers of the structural wavenumber. The Fourier transformation of surface velocities along with its corresponding derivatives is used to derive a mathematical model for estimating acoustic power radiating of a rectangular baffled thin plate under different boundary conditions at low frequencies. The Fourier domain has been used in [15] as a basis for understanding the radiation from wave-chaotic membranes, which have characteristics related to the random-wave scenario of this paper, and is a significant motivation for the analysis of section 4 in particular.

The boundary conditions of a vibrating plate for frequencies below the critical frequency, are known to effect its sound radiation. In calculations, simply supported boundaries are often used because this assumption simplifies the calculations. Several authors have reviewed other boundary conditions for the baffled case [16–19]. For frequencies up to half the critical frequency, Maidanik [16] observed that the radiation efficiency of a clamped plate is 3 dB higher than that of a plate which is simply supported. Leppington *et al* [17] have also proposed that below the critical frequency, the calculation of a simply supported plate should be adjusted to approximately 3 dB for a clamped plate. An extended model for five different kinds of edge conditions, ranging from free to restrained edges has been suggested by Gomperts [18]. Simple approximations were given in this paper for the low-frequency range. Edge-constrained plates are shown to often not have greater radiation efficiencies than those that are less edge-constrained. It was found that a guided plate has a lower radiation efficiency than that of a simply supported plate below the first resonance frequency [18]. A plate with a mixture of simply supported and clamped edges was also found to have about the same radiation efficiency (difference <1 dB) as a plate that is simply supported. Berry *et al* [19] have suggested a formulation for general boundary conditions. By choosing a family of trial functions matching the geometry of the boundary conditions, a Rayleigh–Ritz technique was used. For a single forcing location, the radiation efficiency of multi-modal responses was measured. In the average sense, apart from the antisymmetric resonances occurring for particular cases, the radiation efficiency for clamped and simply supported plates was found to be almost equal. In the case of guided-guided and free-free edges, the same phenomenon was noted. Below the critical frequency and when the modal density is low, Berry *et al* [19] studied the influence of boundary conditions on sound radiation. It is well established that the radiation of sound through a given mode, excited below its modal critical frequency, is due to the edges and corners of the plate for a finite, simply supported, baffled plate [10]. While in free and guided cases the radiation efficiency is almost the same in low order modes, in higher modes the radiation efficiency is considerably larger than in the guided case [20].

In nature, sound radiation from complex structures with wave chaotic vibrational fields is often difficult to estimate using conventional deterministic methods and a stochastic approach may be favourable. In this context, a two-point CF provides the natural characterisation of the structural vibration problem [21]. In the physics and optics literature, CFs have been intensively studied. Berry’s conjecture [22] states that the CF is universal in the presence of ray chaos and is equivalent to correlations of a Gaussian random field [23, 24]. After sufficient averaging, non-universal corrections can be obtained by making a connection between the imaginary part of the Green function of the system and the CF, see [25] for an overview. The CF can in turn be related to ray- and energy-density distributions on the structure based on a structure-borne ray-tracing analysis [1, 26] using Wigner transformation techniques [21].

The focus of this paper is to reinterpret the radiation efficiency for plate-like structures in terms of an integral over a two-point CF for the distribution of vibrational velocities, see also [27]. We will use this formulation to investigate the effect of boundary conditions on sound radiation below the critical frequency in detail. We will do this for a random wave excitation for a planar structure set into an infinite baffle modified near edges to account for boundary conditions. Such diffuse fields are naturally characterised by a two-point CF having the form of a sum over Bessel functions. We consider here extensions of Dirichlet or Neumann boundary conditions to the fourth-order plate equations, which serve as simplified models representing simply supported or guided boundary conditions for bending modes in plates.

The paper is structured as follows. In section 2, we give a short introduction into sound radiation from plates and diffuse waves fields and combine these concepts in an integral expression for the radiation efficiency of finite size plates including boundary conditions. In section 3, we argue that the radiation efficiency has a series expansion similar to the Weyl expansion containing a bulk term and boundary corrections. We give asymptotic results for the boundary term, which is the leading term below the critical frequency. These results are then derived in detail in section 4 based on Fourier representation techniques. We also discuss corner corrections for right angled corners and give explicit results for rectangular plates followed by concluding remarks in section 5.

2. Sound radiation from diffuse field excitation

In the following, we will consider a plate set in an infinite baffle and subject to harmonic excitation of the form $e^{-i\omega t}$ (which is implied throughout the paper) radiating into an air-filled half-space. We present a computation of the sound-radiated power output of a flat structure in terms of the CF of the surface velocities; these CFs appear naturally when considering, for example, the radiation efficiency or radiated power of a structure, but allow for a treatment of stochastic and in particular fully diffuse field excitation.

2.1. Sound power and radiation efficiency

The radiated sound power can be obtained by integrating the acoustic intensity over the surface of the vibrating structure. This surface, denoted Ω , is finite for baffled radiators, covering only the non-baffled field. With $d\mathbf{x} = dx dy$, we can write the total radiated power in the form

$$\Pi = \frac{1}{2} \operatorname{Re} \left\{ \int_{\Omega} p(\mathbf{x}) w^*(\mathbf{x}) d\mathbf{x} \right\}, \quad (1)$$

where $\operatorname{Re}\{\}$ denotes the real part of the expression in brackets, $w(\mathbf{x})$ is the surface velocity at a location $\mathbf{x} = (x, y)$ on the structure, $*$ denotes complex conjugation and $p(\mathbf{x})$ is the acoustic pressure just above the plate.

We use as a basis for our calculation the Kirchoff–Helmholtz equation for irregularly shaped vibrating bodies, which can be further simplified, for planar structures, to the well-known Rayleigh integral [28]. Here the pressure p radiated by a vibrating plate set in an infinite rigid baffle, is at any point $(\mathbf{x}, z) = (x, y, z)$ off-plane given by

$$p(\mathbf{x}, z) = -\frac{i\omega\rho_0}{2\pi} \int_{\Omega} w(\mathbf{x}') \frac{e^{ik_A R}}{R} d\mathbf{x}', \quad (2)$$

where $R = \sqrt{(x - x')^2 + (y - y')^2 + z^2}$, c_0 is the speed of sound in the surrounding medium, ρ_0 is the fluid (air) density and $k_A = \omega/c_0$ denotes the acoustic wavenumber. On taking the limit

$z \rightarrow 0$ to find the sound pressure next to the plate itself, we can express (1) using surface velocities alone [29, 30]. That is,

$$\Pi = \omega \rho_0 \int_{\Omega} \int_{\Omega} g(|\mathbf{x} - \mathbf{x}'|) w(\mathbf{x}) w^*(\mathbf{x}') \, d\mathbf{x} d\mathbf{x}', \quad (3)$$

where

$$g(|\mathbf{x} - \mathbf{x}'|) = \frac{\sin(k_A |\mathbf{x} - \mathbf{x}'|)}{4\pi |\mathbf{x} - \mathbf{x}'|} = \text{Im } G(\mathbf{x}, \mathbf{x}'), \quad (4)$$

in which

$$G(\mathbf{x}, \mathbf{x}') = \frac{e^{-ik_A |\mathbf{x} - \mathbf{x}'|}}{4\pi |\mathbf{x} - \mathbf{x}'|}$$

denotes the free-space acoustic Green function in 3D.

The *radiation efficiency* [2, 7, 8, 10, 29] is defined as the ratio

$$\sigma = \frac{\Pi}{\Pi_0} \quad (5)$$

between the radiated power and an equivalent power

$$\Pi_0 = \frac{1}{2} \rho_0 c_0 \int_{\Omega} |w(\mathbf{x})|^2 \, d\mathbf{x} \quad (6)$$

radiated by a large oscillating piston occupying the surface area $\mathcal{A} = \int_{\Omega} d\mathbf{x}$ and moving with the RMS velocity of the original problem.

In the following sections it will be convenient to work instead with the following *scaled* powers

$$\Pi' = \frac{\Pi}{\frac{1}{2} \rho_0 c_0} \quad \text{and} \quad \Pi'_0 = \frac{\Pi_0}{\frac{1}{2} \rho_0 c_0}.$$

Scaled powers, and quantities derived from them that are similarly scaled, will be denoted using a prime.

2.2. Stationary random fields and diffuse field excitation

Equations (3) and (6) can be generalised to stationary random fields by taking an ensemble average over time intervals, frequency or local spatial averaging, and replacing

$$w(\mathbf{x}) w^*(\mathbf{x}') \rightarrow \langle w(\mathbf{x}) w^*(\mathbf{x}') \rangle \equiv \Gamma_{\Omega}(\mathbf{x}, \mathbf{x}'), \quad (7)$$

where $\Gamma_{\Omega}(\mathbf{x}, \mathbf{x}')$ denotes the velocity CF. Note that $\Gamma_{\Omega}(\mathbf{x}, \mathbf{x}')$ vanishes if \mathbf{x} or \mathbf{x}' are outside of Ω , due to the baffled plate condition. The CF rather than the field amplitude provides a natural way of characterising stationary stochastic fields. Substituting equation (7) into (3), the averaged total radiated (scaled) power can be expressed as

$$\Pi' = 2k_A \int_{\Omega} \int_{\Omega} g(|\mathbf{x} - \mathbf{x}'|) \Gamma_{\Omega}(\mathbf{x}, \mathbf{x}') \, d\mathbf{x} d\mathbf{x}' \quad (8)$$

for a diffuse field, while the denominator in (5) is replaced by

$$\Pi'_0 = \int_{\Omega} \Gamma_{\Omega}(\mathbf{x}, \mathbf{x}) \, d\mathbf{x}. \tag{9}$$

Letting \hat{g} denote the integral operator

$$[\hat{g}w](\mathbf{x}) = 2k_A \int_{\mathbb{R}^2} g(\mathbf{x} - \mathbf{x}')w(\mathbf{x}')d\mathbf{x}', \tag{10}$$

we can then express the scaled powers formally in terms of the following trace operations

$$\Pi' = \text{Tr} \hat{g}\Gamma_{\Omega} \quad \text{and} \quad \Pi'_0 = \text{Tr} \Gamma_{\Omega} \tag{11}$$

and the efficiency defined in (5) can be written as

$$\sigma = \frac{\Pi'}{\Pi'_0} = \frac{\text{Tr} \hat{g}\Gamma_{\Omega}}{\text{Tr} \Gamma_{\Omega}}. \tag{12}$$

This more abstract form will be useful in switching to alternative representations (such as obtained using Fourier transforms) of the solutions in later sections.

In both acoustics and elastodynamics, the concept of a diffuse wave field (or a Gaussian random field) in irregularly formed reverberant bodies plays an important role [25, 31–34]. The statistical properties of diffuse field wave functions are characterised by a two-point CF obtained from the superposition of randomly-oriented plane waves at fixed frequency—the so-called random wave model. The bulk properties of a diffuse field far away from boundaries are characterised by a two-point CF of the form [22]

$$\Gamma_0(\mathbf{x}, \mathbf{x}') = \langle w(\mathbf{x})w^*(\mathbf{x}') \rangle = J_0(k_B|\mathbf{x} - \mathbf{x}'|), \tag{13}$$

where J_0 denotes the zero order Bessel function of the first kind, $\langle \cdot \rangle$ frequency or spatial averaging and k_B the wavenumber for bending modes in the plate.

The model (13) must be modified for finite plates. To account for baffling outside the plate we define

$$\Gamma_{\Omega}^{\text{bulk}}(\mathbf{x}, \mathbf{x}') = \chi_{\Omega}(\mathbf{x})\Gamma_0(\mathbf{x}, \mathbf{x}')\chi_{\Omega}(\mathbf{x}'), \tag{14}$$

where

$$\chi_{\Omega}(\mathbf{x}) = \begin{cases} 1 & \mathbf{x} \in \Omega \\ 0 & \mathbf{x} \notin \Omega \end{cases} \tag{15}$$

is the characteristic function of Ω . In figure 1, a numerical evaluation of the integrals in (12) using the bulk CF (13) for a rectangular domain Ω is shown together with boundary corrections discussed below.

2.3. The importance of boundary conditions

This CF (13) provides a reasonable model for the driving of acoustic radiation from the interior of Ω , but does not adequately account for modifications due to the boundary conditions near the plate edges. A central result of this paper is that these boundary conditions are a leading order effect in acoustic radiation below a critical frequency. A full treatment of generic plate boundary conditions, including common cases such as free edges, is rather complicated to

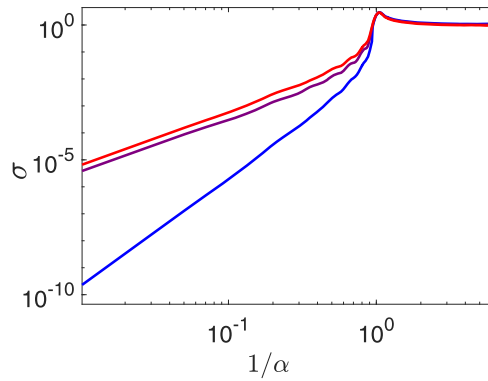


Figure 1. The development of radiation efficiency across the critical frequency (corresponding to $\alpha = 1$) is illustrated for a baffled rectangular plate with $L_x = L_y = 2$, subject to diffuse vibrational-field excitation and for Dirichlet and Neumann boundary conditions. These results have been obtained from a numerical evaluation of the integrals in (12), with CFs of the form given in (16) and with k_B fixed so that $k_B L_y = 42$. Identical results can be obtained using the Fourier-domain approach of section 4. The bulk contribution is plotted in purple here, the red curve includes the boundary corresponds to the Dirichlet case and the blue curve to the Neumann case. Note that the bulk contribution is at leading order the arithmetic mean of the Dirichlet and Neumann cases (see section 4).

treat in this respect, however. We will instead use simplified boundary conditions as a proof-of-principle demonstration of the importance of boundary conditions more generally, and defer a full treatment of arbitrary boundary conditions to future work.

We will treat two particular sets of boundary conditions, which we label *Dirichlet* and *Neumann*. We use this terminology because the eigenfunctions are the same as those in the correspondingly labelled second-order problems of sound radiated by a vibrating membrane, where Dirichlet and Neumann boundary conditions are obtained by setting the solution or its derivative to zero. For the fourth-order plate vibration problem, we should include additional conditions possibly involving the third and fourth derivatives of the wave field on the boundary. The problems we label Dirichlet correspond more properly in the plate-vibration problem to *simply-supported* boundary conditions, in which the solution and its second derivative vanish. The problems we label Neumann represent *guided* boundary conditions in which we set the first and third derivatives to zero. These boundary conditions are chosen because they allow treatment by the method of images.

We separately impose a *baffling* condition outside the plate. This acoustics terminology corresponds physically to enclosing the plate in a rigid, nonvibrating plane and is modelled mathematically by setting the normal acoustic velocity to zero in the exterior of the plate in the plane containing it. It is imposed because it allows us to use the simplified Rayleigh integral (2) to calculate sound pressure. The baffling condition is less physical in the Neumann case, but provides a tractable model for the proof-of-principle demonstration in this paper that boundary conditions are a leading effect.

Correlation functions near a boundary, taking into account boundary conditions, have been described in [35] using a boundary-modified random plane-wave model. Accounting also for baffling, these are written here in the form

$$\Gamma_{\Omega}^{\text{edge}}(\mathbf{x}, \mathbf{x}') = \chi_{\Omega}(\mathbf{x})(J_0(k_B|\mathbf{x} - \mathbf{x}'|) \pm J_0(k_B|\mathbf{x} - \mathcal{R}\mathbf{x}'|))\chi_{\Omega}(\mathbf{x}'), \quad (16)$$

where $\mathcal{R}\mathbf{x}'$ denotes a reflection of \mathbf{x}' through the edge and the \pm signs apply to Neumann and Dirichlet boundary conditions, respectively. For other boundary conditions, the corrections are more complicated and not treatable by the method of images. Instead, one can take the approach described in [35], for example, where random superpositions of plane waves are replaced by random superpositions of sines, cosines but now modified to account for the reflection phases of generic boundary corrections and to include the decaying exponentials present in the solutions of the fourth-order plate equation. In any case, these boundary corrections are valid exactly only in domains with straight edges but we will argue that they give useful approximations near generically shaped boundaries.

A numerical evaluation of the integrals in (12) using the CF (16) including boundary corrections for a rectangular domain Ω is shown in figure 1, here at a wavelength $k_B L_y = 42$. Interestingly, the radiation efficiency for the Dirichlet case is larger than for the Neumann case, an observation to be discussed in more detail in the next sections.

2.4. Critical and subcritical radiation

The radiation efficiency for an infinite flat plate is [36]

$$\sigma = \begin{cases} 0 & \text{for } \alpha > 1, \\ \frac{1}{\sqrt{1 - \alpha^2}} & \text{for } \alpha < 1, \end{cases} \quad (17)$$

with

$$\alpha = \frac{k_B}{k_A}.$$

Because $k_B \propto \sqrt{\omega}$ (see (A.1) [7]) and k_A is linear in frequency, then $\alpha \propto 1/\sqrt{\omega}$ decreases with frequency and there is a critical frequency ω_c , depending on material parameters but not system geometry, where $\alpha = 1$. When $\alpha > 1$, which is the case at low frequencies, the acoustic wave decays evanescently away from the vibrating surface and therefore carries no power, so the radiation efficiency vanishes. At higher frequencies, where $\alpha < 1$, the vibrating surface is an efficient radiator of sound.

The situation changes if the plate is of finite size. Then, a plate also radiates at lower frequencies, where $\alpha > 1$, and a smooth transition occurs across the critical frequency (where $\alpha = 1$) towards the case of efficient bulk radiation for $\alpha < 1$. The aim of this paper is to characterise these finite-size effects for diffuse fields by evaluating (12). For finite domains, the bulk contribution from the interior of Ω dominates the integral in the numerator of equation (12) when $\alpha < 1$ and the plate remains a good radiator. When $\alpha > 1$, the bulk contribution vanishes in the limit of large plates ($\Omega \rightarrow \mathbb{R}^2$) and the integral is then dominated by contributions near the boundary. These arise from two mechanisms: (i) when the integral in the numerator of (12) is truncated, phase cancellations are incomplete near the boundary and (ii) corrections near the boundary such as discussed in equation (16)—and depending on the boundary conditions—give significant contributions. Both of these effects are of the same order.

3. Evaluation of finite-size and boundary effects

We now describe how finite-size and boundary effects enter into the calculation of the radiation efficiency starting from equation (12). It is useful to approach this from two different points of view, respectively doing the calculations in the direct and Fourier domains. We will treat these approaches in turn, in this section and the next.

3.1. Radiation in the direct representation

Let us begin by transforming the integral in the numerator of (12) in terms of the following mean and displacement variables,

$$\bar{\mathbf{x}} = \frac{\mathbf{x} + \mathbf{x}'}{2} \quad \text{and} \quad \mathbf{u} = \mathbf{x} - \mathbf{x}'. \quad (18)$$

Assuming that Ω is convex and \mathbf{x} and \mathbf{x}' are in Ω , then the domain of $\bar{\mathbf{x}}$ is Ω itself, whereas the domain of \mathbf{u} is a set $\Omega_{\bar{\mathbf{x}}}$ depending on $\bar{\mathbf{x}}$. The domain $\Omega_{\bar{\mathbf{x}}}$ is obtained by demanding that both $\mathbf{x} = \bar{\mathbf{x}} + \mathbf{u}/2$ and $\mathbf{x}' = \bar{\mathbf{x}} - \mathbf{u}/2$ are in Ω ; note that the area of $\Omega_{\bar{\mathbf{x}}}$ shrinks to zero as $\bar{\mathbf{x}}$ approaches the boundary of Ω . The numerator in (12) is then of the form

$$\text{Tr } \hat{g}\Gamma_{\Omega} = 2k_A \int_{\Omega} d\bar{\mathbf{x}} \int_{\Omega_{\bar{\mathbf{x}}}} d\mathbf{u} g(\mathbf{u}) \Gamma_{\Omega}(\bar{\mathbf{x}} + \mathbf{u}/2, \bar{\mathbf{x}} - \mathbf{u}/2). \quad (19)$$

For the special case of the diffuse-field bulk CF (14), which is independent of $\bar{\mathbf{x}}$, the integral (19) can be written as

$$\text{Tr } \hat{g}\Gamma_{\Omega}^{\text{bulk}} = k_A \int_{\Omega} d\bar{\mathbf{x}} \int_{\Omega_{\bar{\mathbf{x}}}} d\mathbf{u} \frac{\sin(k_A u)}{2\pi u} J_0(\alpha k_A u), \quad \text{where } u \equiv |\mathbf{u}|.$$

Note that replacing $\Omega_{\bar{\mathbf{x}}} \rightarrow \mathbb{R}^2$ here and transforming to polar coordinates results in the inner integral

$$\begin{aligned} k_A \int_{\mathbb{R}^2} \frac{\sin(k_A u)}{2\pi u} J_0(\alpha k_A u) d\mathbf{u} &= \int_0^{\infty} \sin(\tilde{u}) J_0(\alpha \tilde{u}) d\tilde{u} \\ &= \begin{cases} 0 & \text{for } \alpha > 1, \\ \frac{1}{\sqrt{1 - \alpha^2}} & \text{for } \alpha < 1, \end{cases} \end{aligned}$$

see [37], section 6.67, which is consistent with the infinite plate result (17) after normalising by the plate area \mathcal{A} in (12). For finite plates, incomplete phase cancellation in the corresponding integral over $\Omega_{\bar{\mathbf{x}}}$ leads to a nonzero efficiency for $\alpha > 1$, which is an important part of the finite-size effects discussed later. Note that this is predominantly a boundary effect because $\Omega_{\bar{\mathbf{x}}}$ shrinks as $\bar{\mathbf{x}}$ approaches the boundary.

3.2. Boundary contributions to radiation

To better understand boundary contributions to radiation, we examine a simplified planar geometry illustrated in figure 2. We replace a region near the boundary of Ω , sketched on the left, with a semi-infinite strip in a half-plane, sketched on the right. In the rectified geometry we use Cartesian coordinates $\mathbf{x} = (x, y)$ with x running along the boundary and $0 < y < \infty$. We consider the case $\alpha > 1$, for which the resulting integral is dominated by boundary contributions.

The radiated power from the entire half-plane is infinite, so we regularise the calculation by restricting integration over \bar{x} to a finite interval—when radiation is localised near the boundary of the plate for $\alpha > 1$, this can then be interpreted as providing a radiated power per unit length. We calculate the contribution to (19) for \bar{x} between x and Δx , while u_x ranges over the whole

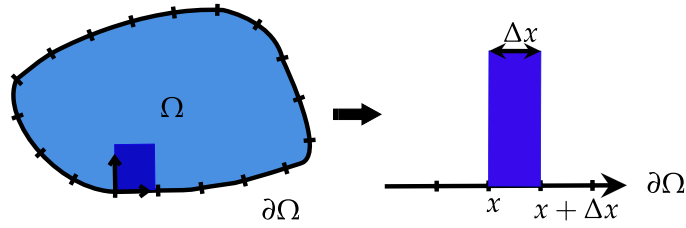


Figure 2. Schematic illustration of the local parameterisation of the plate around its boundary using a rectified geometry.

real line and \bar{y} and u_y are constrained by $0 < y, y' < \infty$. The corresponding contribution to Π' is then

$$\Delta\Pi' = 2k_A \int_x^{x+\Delta x} d\bar{x} \int_0^\infty d\bar{y} \int_{-\infty}^\infty du_x \int_{-2\bar{y}}^{2\bar{y}} du_y g(|\mathbf{u}|) \Gamma_\Omega(\bar{\mathbf{x}} + \mathbf{u}/2, \bar{\mathbf{x}} - \mathbf{u}/2).$$

The inner integrals over u_x and u_y replace the integral over $\Omega_{\bar{\mathbf{x}}}$ in (19); note that the range of the integral over u_y shrinks to zero as $\bar{y} \rightarrow 0$. We further define a (scaled) radiated power per unit length by

$$\pi'(x) \equiv \frac{\Delta\Pi'}{\Delta x} = 2k_A \int_0^\infty d\bar{y} \int_{-\infty}^\infty du_x \int_{-2\bar{y}}^{2\bar{y}} du_y g(|\mathbf{u}|) \Gamma_\Omega(\bar{\mathbf{x}} + \mathbf{u}/2, \bar{\mathbf{x}} - \mathbf{u}/2). \quad (20)$$

This integral converges when $\alpha > 1$, and is dominated by contributions that are confined to an increasingly narrow layer in \bar{y} in the asymptotic limit $k_A \rightarrow \infty$. We may use this as the basis for an asymptotic approximation for the radiation efficiency in the form of a boundary integral

$$\sigma \simeq \frac{\int_{\partial\Omega} \pi'(s) ds}{\int_\Omega \Gamma_\Omega(\mathbf{x}, \mathbf{x}) d\mathbf{x}},$$

where the arclength s replaces x in the full geometry. Note that, even for $\alpha > 1$, the denominator here is dominated by bulk contributions, and is equal to the area \mathcal{A} of the plate for the CF in (14), for example. The approach taken here is motivated by established derivations of the Weyl formula for the density of states of billiard problems, where bulk and boundary terms can likewise be obtained from free-space Green functions and their image corrections, respectively [3–5]. In the current case, when $\alpha > 1$, however, the bulk contribution vanishes and the Weyl-formula analogue begins with the boundary contribution.

In the special case where $\Gamma_\Omega(\mathbf{x}, \mathbf{x}')$ is of the form (16), we find that the remaining integral transverse to the boundary depends on the boundary conditions but is independent of s and other geometrical features, so that,

$$\begin{aligned} \sigma &\simeq \frac{1}{\mathcal{A}} \int_{\partial\Omega} ds \times \text{integrals independent of geometry} \\ &\equiv \frac{2\ell}{\pi k_A \mathcal{A}} f(\alpha), \end{aligned} \quad (21)$$

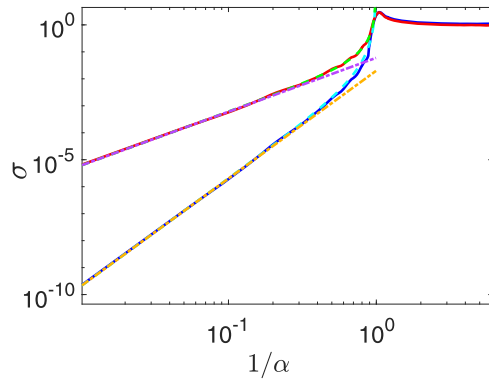


Figure 3. The radiation efficiency for a baffled rectangular plate with side lengths L_x and L_y subject to diffuse vibrational excitation and for Dirichlet and Neumann boundary conditions for $L_y K_B = 42$. Results from a numerical simulation as shown in figure 1 are compared with the approximations evaluated using (21) together with (22) (green dashed curve for the Dirichlet case and cyan dashed curve for the Neumann case) and using the asymptotic form (23) (purple dot-dashed curve for Dirichlet and gold dot-dashed curve for Neumann).

where ℓ denotes the perimeter of Ω and

$$f(\alpha) = \frac{1}{2\pi} \int_0^{2\pi} d\phi \int_0^1 dp \frac{p}{\sqrt{1-p^2} \sqrt{\alpha^2 - p^2 \cos^2 \phi}} \begin{cases} \frac{\alpha^2 - p^2 \cos^2 \phi}{(\alpha^2 - p^2)^2} & \text{Dirichlet,} \\ \frac{p^2 \sin^2 \phi}{(\alpha^2 - p^2)^2} & \text{Neumann.} \end{cases} \quad (22)$$

The form given here for $f(\alpha)$ is derived in the following sections.

The asymptotic result (21) is compared in figure 3 with direct evaluation of (12), which has previously been shown in figure 1: the asymptotic approximation and full evaluation agree well for $\alpha > 1$ except as α approaches the critical value $\alpha = 1$, where it is expected that the asymptotic approximation should fail. There are also some small oscillations not accounted for by this asymptotic result—these are eliminated after some frequency averaging, for example, as set out in appendix A. We also show in appendix A that, in the rectangular case where modes can be calculated analytically, these diffuse-field results are successfully reproduced by a modal average (see figure A2).

Interestingly, we find in all these cases that the radiation efficiency for the Dirichlet case is larger than for the Neumann case below the critical frequency, for otherwise identical geometries. This observation can be highlighted by evaluating the asymptotic form of $f(\alpha)$ as $\alpha \rightarrow \infty$:

$$f(\alpha) \simeq \begin{cases} \frac{1}{\alpha^3} & \text{Dirichlet,} \\ \frac{1}{3\alpha^5} & \text{Neumann} \end{cases} \quad (23)$$

(and see also figure 3). A derivation of (23) is given in appendix C.

The observation of relatively higher radiated power for the Dirichlet case is somewhat counterintuitive as the velocity amplitude driving the radiated power in (11) must vanish on the boundary for those boundary conditions, but is typically nonzero in the Neumann case. Given

that acoustic radiation for $\alpha > 1$ originates from contributions near the boundaries of a plate, one might expect intuitively that the Neumann case with non-zero amplitude on the boundary would be the more efficient radiator. Why this is not the case is not immediately clear from the integral in (12), but emerges from the more detailed calculations to follow. It stems ultimately from the fact that radiation is effectively from a boundary layer several wavelengths deep and the value of the solution at the terminating edge of the layer does not determine the overall contribution in a simple way.

4. Finite size effects using a Fourier representation

Fourier representation provides a useful means of interpreting and calculating the radiated power discussed in the previous sections. It has been used in [15], for example, where a more detailed discussion can be found of the challenges and uses of the method.

4.1. Radiation in the Fourier domain

We transform to a Fourier representation using the convention

$$\mathcal{F}[w(\mathbf{x})] = W(\mathbf{p}) = \int_{\mathbb{R}^2} e^{-ik_A \mathbf{p} \cdot \mathbf{x}} w(\mathbf{x}) d\mathbf{x}. \tag{24}$$

Note that even though the plate is confined to the domain Ω , we define the Fourier transform over the whole plane in general and rely on the baffling conditions $w(\mathbf{x}) = 0$ for $\mathbf{x} \notin \Omega$ to reduce this to

$$W(\mathbf{p}) = \int_{\Omega} e^{-ik_A \mathbf{p} \cdot \mathbf{x}} w(\mathbf{x}) d\mathbf{x}$$

when appropriate. We also use the acoustic wavenumber k_A in (24) even when dealing with the vibrational problem. The transform of the two-point CF (7) is correspondingly defined by

$$\mathcal{F}[\Gamma_{\Omega}(\mathbf{x}, \mathbf{x}')] = \Gamma_{\Omega}(\mathbf{p}, \mathbf{p}') = \int_{\mathbb{R}^2} \int_{\mathbb{R}^2} e^{-ik_A \mathbf{p} \cdot \mathbf{x} + ik_A \mathbf{p}' \cdot \mathbf{x}'} \Gamma_{\Omega}(\mathbf{x}, \mathbf{x}') d\mathbf{x} d\mathbf{x}'.$$

Fourier representation is useful because it simplifies the operator \hat{g} appearing in the integral (12), being defined as the convolution integral (10). We first note that the Fourier transform of the kernel defined in (4) is

$$\begin{aligned} \mathcal{F}[g(\mathbf{x})] &= \frac{1}{2k_A} \begin{cases} \frac{1}{\sqrt{1 - |\mathbf{p}|^2}} & \text{for } |\mathbf{p}| < 1 \\ 0 & \text{for } |\mathbf{p}| > 1 \end{cases} \\ &\equiv \frac{1}{2k_A} K(\mathbf{p}), \end{aligned}$$

see [37], section 6.67. Then

$$\mathcal{F}[\hat{g}w] = K(\mathbf{p})W(\mathbf{p})$$

vanishes outside the disk D defined by $|\mathbf{p}| < 1$. Furthermore the trace operations in (11) and (12) can respectively be confined to diagonal components inside the disk D :

$$\Pi' = \left(\frac{k_A}{2\pi}\right)^2 \int_{\mathbb{R}^2} K(\mathbf{p})\Gamma_{\Omega}(\mathbf{p}, \mathbf{p}) d\mathbf{p} = \left(\frac{k_A}{2\pi}\right)^2 \int_D \frac{\Gamma_{\Omega}(\mathbf{p}, \mathbf{p})}{\sqrt{1 - |\mathbf{p}|^2}} d\mathbf{p} \tag{25}$$

and

$$\sigma = \frac{\int_D \frac{\Gamma_\Omega(\mathbf{p}, \mathbf{p})}{\sqrt{1 - |\mathbf{p}|^2}} d\mathbf{p}}{\int_{\mathbb{R}^2} \Gamma_\Omega(\mathbf{p}, \mathbf{p}) d\mathbf{p}}. \tag{26}$$

The radiation efficiency is thus an average of the function $K(\mathbf{p})$ weighted by $\Gamma_\Omega(\mathbf{p}, \mathbf{p})$.

The infinite plate limit (17), and the origin of deviations due to finite-size effects are easily understood qualitatively from this form. When the vibrational field is characterised by the wave number k_B , the diagonal Fourier elements $\Gamma_\Omega(\mathbf{p}, \mathbf{p})$ are supported near the circle in \mathbf{p} space given by the condition

$$|\mathbf{p}| = \alpha \equiv \frac{k_B}{k_A}$$

(see also the discussion in the next section). If we take a limit in which Ω gets larger, this support concentrates in an increasingly narrow neighbourhood of the circle $|\mathbf{p}| = \alpha$, converging to the δ function in equation (32) below. If $\alpha < 1$, the narrowing support of $\Gamma_\Omega(\mathbf{p}, \mathbf{p})$ lies inside the support D of $K(\mathbf{p})$ and we find the nonzero limit

$$\sigma \rightarrow \frac{1}{\sqrt{1 - \alpha^2}} \quad \text{for } \mathcal{A} \rightarrow \infty.$$

If $\alpha > 1$, then the support of $\Gamma_\Omega(\mathbf{p}, \mathbf{p})$ increasingly concentrates outside of D and

$$\sigma \rightarrow 0 \quad \text{for } \mathcal{A} \rightarrow \infty.$$

Finite-size effects at moderate plate sizes are then determined by the part of $\Gamma_\Omega(\mathbf{p}, \mathbf{p})$ overlapping with the disk D .

4.2. Accounting for the plate geometry in the Fourier domain

In order to incorporate the plate geometry in a Fourier representation of the radiation problem, let us define

$$H(\mathbf{p}) = \int_{\mathbb{R}^2} \chi_\Omega(\mathbf{x}) e^{-ik_A \mathbf{p} \cdot \mathbf{x}} d\mathbf{x} = \int_\Omega e^{-ik_A \mathbf{p} \cdot \mathbf{x}} d\mathbf{x}, \tag{27}$$

where $\chi_\Omega(\mathbf{x})$ is the characteristic function of Ω as defined in (15). Then the Fourier transform of the CF in (16) can be written

$$\Gamma_\Omega^{\text{edge}}(\mathbf{p}, \mathbf{p}') = A(\mathbf{p}, \mathbf{p}') \pm B(\mathbf{p}, \mathbf{p}'), \tag{28}$$

where the lead term is a double convolution

$$\begin{aligned} A(\mathbf{p}, \mathbf{p}') &= \left(\frac{k_A}{2\pi}\right)^4 \int H(\mathbf{p} - \mathbf{q}) \Gamma_0(\mathbf{q}, \mathbf{q}') H(\mathbf{p}' - \mathbf{q}') d\mathbf{q} d\mathbf{q}' \\ &\equiv \left(\frac{k_A}{2\pi}\right)^4 H(\mathbf{p}) * \Gamma_0(\mathbf{p}, \mathbf{p}') * H(\mathbf{p}'), \end{aligned} \tag{29}$$

with

$$\Gamma_0(\mathbf{p}, \mathbf{p}') = \int_{\mathbb{R}^2} \int_{\mathbb{R}^2} J_0(\alpha k_A |\mathbf{x} - \mathbf{x}'|) e^{-ik_A \mathbf{p} \cdot \mathbf{x} + ik_A \mathbf{p}' \cdot \mathbf{x}'} d\mathbf{x} d\mathbf{x}' \tag{30}$$

and the image contribution $B(\mathbf{p}, \mathbf{p}')$ is discussed in more detail below. Note that $\Gamma_0(\mathbf{p}, \mathbf{p}')$ is defined by a Fourier transform over all of \mathbb{R}^2 and is independent of the plate geometry, which is encoded in the convolution with $H(\mathbf{p})$.

4.3. Contribution from the bulk

In order to further simplify this result, let us define mean and displacement variables, in analogy with (18), according to

$$\bar{\mathbf{p}} = \frac{\mathbf{p} + \mathbf{p}'}{2} \quad \text{and} \quad \mathbf{q} = \mathbf{p} - \mathbf{p}'. \tag{31}$$

Then equation (30) yields

$$\hat{\Gamma}_0(\bar{\mathbf{p}} + \mathbf{q}/2, \bar{\mathbf{p}} - \mathbf{q}/2) = \int_{\mathbb{R}^2} \int_{\mathbb{R}^2} J_0(\alpha k_A |\mathbf{u}|) e^{-ik_A \mathbf{q} \cdot \bar{\mathbf{x}} - ik_A \bar{\mathbf{p}} \cdot \mathbf{s}} \, d\mathbf{u} \, d\bar{\mathbf{x}} \tag{32}$$

$$= \frac{1}{\pi} \left(\frac{2\pi}{k_A} \right)^4 \delta(\mathbf{q}) \delta(|\bar{\mathbf{p}}|^2 - \alpha^2). \tag{33}$$

Inserting this into (29) gives

$$\begin{aligned} A(\mathbf{p}, \mathbf{p}') &= \frac{1}{\pi} \int_{\mathbb{R}^2} d\mathbf{p}'' \, H(\mathbf{p} - \mathbf{p}'') \delta(|\bar{\mathbf{p}}|^2 - \alpha^2) H^*(\mathbf{p}' - \mathbf{p}'') \\ &= \langle H(\mathbf{p} - \mathbf{p}_\alpha) H^*(\mathbf{p}' - \mathbf{p}_\alpha) \rangle, \end{aligned} \tag{34}$$

where $\mathbf{p}_\alpha(\theta) = (\alpha \cos \theta, \alpha \sin \theta)$ and the average $\langle \cdot \rangle$ is over the direction of \mathbf{p}_α .

Substituting the definition (27) for $H(\mathbf{p})$ and transforming to mean and displacement coordinates as in (19) allows us to write this in the form

$$\begin{aligned} A(\mathbf{p}, \mathbf{p}') &= \left\langle \int_{\Omega} \int_{\Omega} e^{-ik_A(\mathbf{p} - \mathbf{p}_\alpha) \cdot \mathbf{x}} e^{ik_A(\mathbf{p}' - \mathbf{p}_\alpha) \cdot \mathbf{x}'} \, d\mathbf{x} \, d\mathbf{x}' \right\rangle \\ &= \left\langle \int_{\Omega} d\bar{\mathbf{x}} \int_{\Omega_{\bar{\mathbf{x}}}} d\mathbf{u} \, e^{-ik_A \mathbf{q} \cdot \bar{\mathbf{x}} - ik_A(\bar{\mathbf{p}} - \mathbf{p}_\alpha) \cdot \mathbf{u}} \right\rangle. \end{aligned} \tag{35}$$

Note that for (12) we need only the diagonal elements

$$A(\mathbf{p}, \mathbf{p}) = \left\langle \int_{\Omega} d\bar{\mathbf{x}} \int_{\Omega_{\bar{\mathbf{x}}}} d\mathbf{u} \, e^{-ik_A(\mathbf{p} - \mathbf{p}_\alpha) \cdot \mathbf{u}} \right\rangle$$

obtained by setting $\mathbf{q} = \mathbf{0}$ and $\bar{\mathbf{p}} = \mathbf{p}$, which we may write in the form

$$A(\mathbf{p}, \mathbf{p}) = \int_{\Omega} \langle h_{\bar{\mathbf{x}}}(\mathbf{p} - \mathbf{p}_\alpha) \rangle d\bar{\mathbf{x}}, \tag{36}$$

where

$$h_{\bar{\mathbf{x}}}(\mathbf{p}) \equiv \int_{\Omega_{\bar{\mathbf{x}}}} e^{-ik_A \mathbf{p} \cdot \mathbf{u}} \, d\mathbf{u} \tag{37}$$

(which depends on $\bar{\mathbf{x}}$ because $\Omega_{\bar{\mathbf{x}}}$ does). When $\bar{\mathbf{x}}$ is in the interior of Ω , $h_{\bar{\mathbf{x}}}(\mathbf{p})$ becomes localised around $\mathbf{p} = 0$ as $k_A \rightarrow \infty$. The rate at which this localisation occurs slows as $\bar{\mathbf{x}}$ approaches the boundary of Ω and $\Omega_{\bar{\mathbf{x}}}$ shrinks. Correspondingly, the contribution from $\bar{\mathbf{x}}$ to (36) becomes

increasingly localised around a circle of radius α as discussed in section 4.1. When $\alpha > 0$ this contribution is localised outside the domain of integration in the radiation integral in the numerator of (26) and the radiated power is small. The largest contributions come from values of $\bar{\mathbf{x}}$ near the boundary of Ω , where $h_{\bar{\mathbf{x}}}(\mathbf{p})$ is least localised. These contributions cannot easily be separated however from image-corrections accounting for boundary conditions, which are discussed in the next subsection.

4.4. Contribution from images

To account for the image corrections controlled by the boundary conditions and described by the term $B(\mathbf{p}, \mathbf{p}')$ in (28), we return to the boundary rectification illustrated in figure 2. Here the image contribution in brackets in (16) can be written

$$\Gamma_1(\mathbf{x}, \mathbf{x}') = J_0(\alpha k_A |(x - x', y + y')|)$$

and we define a corresponding Fourier transform

$$\hat{\Gamma}_1(\mathbf{p}, \mathbf{p}') = \int_{\mathbb{R}^2} \int_{\mathbb{R}^2} J_0(\alpha k_A |(x - x', y + y')|) e^{-ik_A \mathbf{p} \cdot \mathbf{x} + ik_A \mathbf{p}' \cdot \mathbf{x}'} \, d\mathbf{x} \, d\mathbf{x}'. \quad (38)$$

As with the equivalent bulk function $\Gamma_0(\mathbf{x}, \mathbf{x}')$, this is defined over the whole plane and does not incorporate the geometry of the plate, which is instead achieved by convolution operations equivalent to (29). That is,

$$B(\mathbf{p}, \mathbf{p}') = \left(\frac{k_A}{2\pi}\right)^4 H(\mathbf{p}) * \Gamma_1(\mathbf{p}, \mathbf{p}') * H(\mathbf{p}'). \quad (39)$$

Using mean and displacement variables (18) in equation (38), we get

$$\begin{aligned} \hat{\Gamma}_1(\bar{\mathbf{p}} - \mathbf{q}/2, \bar{\mathbf{p}} + \mathbf{q}/2) &= \int_{\mathbb{R}^2} \int_{\mathbb{R}^2} J_0(\alpha k_A \sqrt{u_x^2 + (2\bar{y})^2}) e^{-ik_A \mathbf{q} \cdot \bar{\mathbf{x}} - ik_A \bar{\mathbf{p}} \cdot \mathbf{u}} \, d\mathbf{u} \, d\bar{\mathbf{x}}, \\ &= \left(\frac{2\pi}{k_A}\right)^2 \delta(q_x) \delta(\bar{p}_y) \\ &\quad \times \int_{\mathbb{R}^2} J_0(\alpha k_A \sqrt{u_x^2 + (2\bar{y})^2}) e^{-ik_A q_y \bar{y} - ik_A \bar{p}_x u_x} \, du_x \, d\bar{y}. \end{aligned}$$

Making use of the relation [38]

$$J_0(\alpha \sqrt{x^2 + y^2}) = \frac{1}{2\pi} \int_0^{2\pi} d\theta \cos(\alpha x \cos \theta) \cos(\alpha y \sin \theta),$$

we obtain

$$\hat{\Gamma}_1(\bar{\mathbf{p}} - \mathbf{q}/2, \bar{\mathbf{p}} + \mathbf{q}/2) = \frac{1}{2\pi} \left(\frac{2\pi}{k_A}\right)^4 \delta(q_x) \delta(\bar{p}_y) \delta\left(\bar{p}_x^2 + \left(\frac{q_y}{2}\right)^2 - \alpha^2\right). \quad (40)$$

Using similar steps as in the calculation for $A(\mathbf{p}, \mathbf{p}')$, we can simplify $B(\mathbf{p}, \mathbf{p}')$ as follows:

$$B(\mathbf{p}, \mathbf{p}') = \frac{1}{\pi} \int_{\mathbb{R}^2} d\mathbf{p}'' H(\mathbf{p} - \mathbf{p}'') \delta(p_x''^2 + p_y''^2 - \alpha^2) H^*(p_x' - p_x'', p_y' + p_y'').$$

Converting $\mathbf{p}'' = (p'_x, p'_y)$ to polar coordinates yields

$$B(\mathbf{p}, \mathbf{p}') = \langle H(\mathbf{p} - \mathbf{p}_\alpha) H^*(p'_x - \alpha \cos \theta, p'_y + \alpha \sin \theta) \rangle, \tag{41}$$

where the average is over the polar angle of \mathbf{p}_α as for the bulk contributions.

We proceed in analogy to the calculation for $A(\mathbf{p}, \mathbf{p}')$ by writing

$$\begin{aligned} B(\mathbf{p}, \mathbf{p}') &= \left\langle \int_{\Omega} \int_{\Omega} e^{-ik_A(\mathbf{p}-\mathbf{p}_\alpha)\cdot\mathbf{x}} e^{ik_A[(p'_x-\alpha \cos \theta)x'+(p'_y+\alpha \sin \theta)y']} d\mathbf{x} d\mathbf{x}' \right\rangle \\ &= \left\langle \int_{\Omega} d\bar{\mathbf{x}} \int_{\Omega_{\bar{\mathbf{x}}}} d\mathbf{u} e^{-ik_A[(p_x-p'_x)\bar{x}+(p_y-p'_y-2\alpha \sin \theta)\bar{y}]} \right. \\ &\quad \left. \times e^{-ik_A\left[\left(\frac{p_x+p'_x}{2}-\alpha \cos \theta\right)u_x+\left(\frac{p_y+p'_y}{2}\right)u_y\right]} \right\rangle. \end{aligned}$$

The diagonal elements of this can be written in the form

$$B(\mathbf{p}, \mathbf{p}) = \left\langle \int_{\Omega} d\bar{\mathbf{x}} \int_{\Omega_{\bar{\mathbf{x}}}} d\mathbf{u} e^{2ik_A\alpha\bar{y} \sin \theta} e^{-ik_A[(p_x-\alpha \cos \theta)u_x+p_yu_y]} \right\rangle. \tag{42}$$

We will demonstrate in the next section that $B(\mathbf{p}, \mathbf{p})$ is a negative quantity when $\alpha > 1$, so that Dirichlet problems radiate more strongly than Neumann problems for equivalent geometries.

4.5. Evaluation of asymptotic boundary corrections

We now adapt the calculations of sections 4.3 and 4.4 to evaluate the asymptotic boundary contributions to the infinite half-plane scenario in section 3.2. Throughout this subsection it is assumed that $\alpha > 1$ and we consider the limit $k_A \rightarrow \infty$.

Equation (20) can be evaluated by adapting (26) to the rectified geometry of section 3.2. This is achieved by replacing the spatial domains of integration according to

$$(\mathbf{x}, \mathbf{x}') \in \Omega \times \Omega \quad \rightarrow \quad (\bar{x}, u_x, \bar{y}, u_y) \in \mathcal{I} \times \mathbb{R} \times W,$$

where \mathcal{I} is an interval of length Δx and W is the wedge in the (\bar{y}, u_y) -plane defined by $\bar{y} > 0$ and $-2\bar{y} < u_y < 2\bar{y}$. Combining (36) and (42) for this geometry, we write

$$\Gamma_{\Omega}^{\text{edge}}(\mathbf{p}, \mathbf{p}) = \int_{\partial\Omega} (a_{\bar{x}}(\mathbf{p}) \pm b_{\bar{x}}(\mathbf{p})) d\bar{x},$$

where

$$a_{\bar{x}}(\mathbf{p}) = \left\langle \int_0^{\infty} d\bar{y} \int_{-2\bar{y}}^{2\bar{y}} du_y \int_{-\infty}^{\infty} du_x e^{-ik_A[(p_x-\alpha \cos \theta)u_x+(p_y-\alpha \sin \theta)u_y]} \right\rangle$$

and

$$b_{\bar{x}}(\mathbf{p}) = \left\langle \int_0^{\infty} d\bar{y} \int_{-2\bar{y}}^{2\bar{y}} du_y \int_{-\infty}^{\infty} du_x e^{-ik_A[(p_x-\alpha \cos \theta)u_x+p_yu_y-2\alpha\bar{y} \sin \theta]} \right\rangle.$$

These integrals converge when $\alpha > 1$, where the outer integral over \bar{y} becomes increasingly localised near the boundary $\bar{y} = 0$ as $k_A \rightarrow \infty$. This suggests that

$$\pi'(\bar{x}) = \left(\frac{k_A}{2\pi}\right)^2 \int_{\mathbb{R}^2} K(\mathbf{p})(a_{\bar{x}}(\mathbf{p}) \pm b_{\bar{x}}(\mathbf{p})) d\mathbf{p} \tag{43}$$

should be interpreted as a (scaled) radiated power per unit length, providing an alternative means of evaluating (20).

We first compute $a_{\bar{x}}(\mathbf{p})$, which arises from incomplete cancellation of the bulk contribution when integrated over a truncated domain. This term can be rewritten in the form

$$\begin{aligned}
 a_{\bar{x}}(\mathbf{p}) &= \left\langle \int_0^\infty dy \int_0^\infty dy' \int_{-\infty}^\infty du_x e^{-ik_A[(p_x - \alpha \cos \theta)u_x - ik_A(p_y - \alpha \sin \theta)(y - y')] } \right\rangle \\
 &= \left\langle \frac{1}{ik_A(p_y - \alpha \sin \theta - i0^+)} \times \frac{1}{-ik_A(p_y - \alpha \sin \theta + i0^+)} \right. \\
 &\quad \left. \times \frac{2\pi}{k_A} \delta(p_x - \alpha \cos \theta) \right\rangle \\
 &= \frac{1}{k_A^3} \int_0^{2\pi} \frac{1}{(p_y - \alpha \sin \theta)^2} \delta(p_x - \alpha \cos \theta) d\theta \\
 &= \frac{1}{k_A^3} \frac{1}{\sqrt{\alpha^2 - p_x^2}} \left[\frac{1}{(p_y - \sqrt{\alpha^2 - p_x^2})^2} + \frac{1}{(p_y + \sqrt{\alpha^2 - p_x^2})^2} \right] \\
 &= \frac{2}{k_A^3} \frac{1}{\sqrt{\alpha^2 - p_x^2}} \frac{\alpha^2 - p_x^2 + p_y^2}{(\alpha^2 - p_x^2 - p_y^2)^2}. \tag{44}
 \end{aligned}$$

Note that the denominators here cannot vanish for $\alpha > 1$ inside the support of $K(\mathbf{p})$ in (43).

The second contribution $\pm b_{\bar{x}}(\mathbf{p})$ arises due to boundary corrections. It can analogously be written as

$$\begin{aligned}
 b_{\bar{x}}(\mathbf{p}) &= \left\langle \int_0^\infty dy \int_0^\infty dy' \int_{-\infty}^\infty du_x \right. \\
 &\quad \left. \times e^{-ik_A[(p_x - \alpha \cos \theta)u_x + (p_y - \alpha \sin \theta)y - (p_y + \alpha \sin \theta)y'] } \right\rangle \\
 &= \left\langle \frac{1}{ik_A(p_y - \alpha \sin \theta - i0^+)} \times \frac{1}{-ik_A(p_y + \alpha \sin \theta + i0^+)} \right. \\
 &\quad \left. \times \frac{2\pi}{k_A} \delta(p_x - \alpha \cos \theta) \right\rangle \\
 &= \frac{1}{k_A^3} \int_0^{2\pi} \frac{1}{p_y^2 - \alpha^2 \sin^2 \theta} \delta(p_x - \alpha \cos \theta) d\theta \\
 &= -\frac{2}{k_A^3} \frac{1}{\sqrt{\alpha^2 - p_x^2}} \frac{1}{\alpha^2 - p_x^2 - p_y^2}. \tag{45}
 \end{aligned}$$

We thus obtain

$$a_{\bar{x}}(\mathbf{p}) \pm b_{\bar{x}}(\mathbf{p}) = \frac{4}{k_A^3} \frac{1}{\sqrt{\alpha^2 - p_x^2}} \frac{1}{(\alpha^2 - p_x^2 - p_y^2)^2} \times \begin{cases} \alpha^2 - p_x^2 & \text{Dirichlet} \\ p_y^2 & \text{Neumann.} \end{cases}$$

Evaluation of the resulting integrals in (43) using polar coordinates leads to (22).

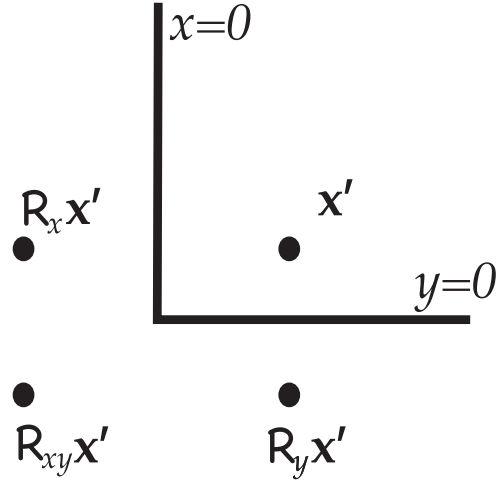


Figure 4. A schematic illustration of the images used to calculate the boundary corrections around a single corner in section 4.7.

4.6. Corner corrections

For the special case of rectangular plate geometries, we can go beyond the bulk and edge contributions considered so far to include also corner corrections arising from image of image contributions as depicted in figure 4. To do so, we need to replace the CF in (16) by

$$\begin{aligned} \Gamma(\mathbf{x}, \mathbf{x}') &= J_0(k_B|\mathbf{x} - \mathbf{x}'|) \pm J_0(k_B|\mathbf{x} - \mathcal{R}_y\mathbf{x}'|) \\ &\quad \pm J_0(k_B|\mathbf{x} - \mathcal{R}_x\mathbf{x}'|) + J_0(k_B|\mathbf{x} - \mathcal{R}_{xy}\mathbf{x}'|) \\ &\equiv \Gamma_0(\mathbf{x}, \mathbf{x}') \pm \Gamma_1(\mathbf{x}, \mathbf{x}') \pm \Gamma_2(\mathbf{x}, \mathbf{x}') + \Gamma_3(\mathbf{x}, \mathbf{x}') \end{aligned} \quad (46)$$

to account for boundary corrections near a corner joining edges $x = y = 0$ (see figure 4). Here, $\mathcal{R}_x\mathbf{x}'$ denotes a reflection of \mathbf{x}' through the edge $x = 0$, $\mathcal{R}_y\mathbf{x}'$ denotes a reflection of \mathbf{x}' through the edge $y = 0$, $\mathcal{R}_{xy} = \mathcal{R}_x\mathcal{R}_y$ and the \pm signs account for Dirichlet and Neumann boundary conditions as before. Contributions $\Gamma_0(\mathbf{x}, \mathbf{x}')$, $\Gamma_1(\mathbf{x}, \mathbf{x}')$ and $\Gamma_2(\mathbf{x}, \mathbf{x}')$ are as given in sections 4.3–4.5 with Γ_2 being a perimeter contribution consistent with the treatment leading to (22). The remaining contribution can be written explicitly as

$$\Gamma_3(\mathbf{x}, \mathbf{x}') = J_0(\alpha k_A|\mathbf{x} + \mathbf{x}'|). \quad (47)$$

We accordingly generalise the contributions of these two edges to the Fourier transform (28) to

$$\Gamma_\Omega^{\text{corner}}(\mathbf{p}, \mathbf{p}') = A(\mathbf{p}, \mathbf{p}') \pm B_1(\mathbf{p}, \mathbf{p}') \pm B_2(\mathbf{p}, \mathbf{p}') + C(\mathbf{p}, \mathbf{p}'), \quad (48)$$

where (see appendix B)

$$C(\mathbf{p}, \mathbf{p}') = \langle H(\mathbf{p} - \mathbf{p}_\alpha)H^*(\mathbf{p}' + \mathbf{p}_\alpha) \rangle. \quad (49)$$

It is shown in appendix B that the corner contribution $C(\mathbf{p}, \mathbf{p}')$ vanishes for 90° corners; a general treatment for arbitrary angles or curvature corrections is not attempted in this paper.

4.7. Radiation from rectangles

We further illustrate the results of sections 4.3–4.6 by applying them to the case of rectangular geometries, for which analytical results are available for the characteristic function $H(\mathbf{p})$ and there are multiple images obtained by reflection through different sides. Although the full solution to this problem is obtained from an infinite sequence of images, we here calculate the contributions only from singly-reflected images from horizontal and vertical sides and doubly-reflected images giving corrections near corners.

For a rectangular plate occupying $0 < x < L_x$ and $0 < y < L_y$, the characteristic function $H(\mathbf{p})$ can be written explicitly as

$$H(\mathbf{p}) = L_x L_y \operatorname{sinc}\left(\frac{1}{2} k_A L_x p_x\right) \operatorname{sinc}\left(\frac{1}{2} k_A L_y p_y\right) e^{-i k_A (p_x L_x + p_y L_y) / 2}.$$

Then the bulk contribution in (34) can be written for $\mathbf{p} = \mathbf{p}'$ as

$$A(\mathbf{p}, \mathbf{p}) = \left\langle \left[\operatorname{sinc}\left(\frac{k_A L_x (p_x - \alpha \cos \theta)}{2}\right) \operatorname{sinc}\left(\frac{k_A L_y (p_y - \alpha \sin \theta)}{2}\right) \right]^2 \right\rangle,$$

whereas the corresponding boundary contribution (41) for the bottom horizontal edge can be written

$$B_1(\mathbf{p}, \mathbf{p}) = \left\langle \left[\operatorname{sinc}\left(\frac{k_A L_x (p_x - \alpha \cos \theta)}{2}\right) \right]^2 \operatorname{sinc}\left(\frac{k_A L_y (p_y - \alpha \sin \theta)}{2}\right) \times \operatorname{sinc}\left(\frac{k_A L_y (p_y + \alpha \sin \theta)}{2}\right) e^{2i \alpha k_A L_y \sin \theta} \right\rangle.$$

Note that there is an analogous contribution

$$B_2(\mathbf{p}, \mathbf{p}) = \left\langle \operatorname{sinc}\left(\frac{k_A L_x (p_x - \alpha \cos \theta)}{2}\right) \operatorname{sinc}\left(\frac{k_A L_x (p_x + \alpha \cos \theta)}{2}\right) \times \left[\operatorname{sinc}\left(\frac{k_A L_y (p_y - \alpha \sin \theta)}{2}\right) \right]^2 e^{2i \alpha k_A L_x \cos \theta} \right\rangle$$

from image corrections along the left vertical edge. Finally, we can also include a corner correction from the bottom left corner using

$$C(\mathbf{p}, \mathbf{p}) = \left\langle \operatorname{sinc}\left(\frac{k_A L_x (p_x - \alpha \cos \theta)}{2}\right) \operatorname{sinc}\left(\frac{k_A L_y (p_y - \alpha \sin \theta)}{2}\right) \times \operatorname{sinc}\left(\frac{k_A L_x (p_x + \alpha \cos \theta)}{2}\right) \operatorname{sinc}\left(\frac{k_A L_y (p_y + \alpha \sin \theta)}{2}\right) \times e^{2i \alpha k_A (L_x \cos \theta + L_y \sin \theta)} \right\rangle.$$

Note that the remaining two sides and three corners contribute symmetrically so that we can account for all four edges and all four corners of the rectangle by using

$$\Gamma_{\Omega}^{\text{rect}}(\mathbf{p}, \mathbf{p}) = A(\mathbf{p}, \mathbf{p}) \pm 2B_1(\mathbf{p}, \mathbf{p}) \pm 2B_2(\mathbf{p}, \mathbf{p}) + 4C(\mathbf{p}, \mathbf{p}) \tag{50}$$

in place of $\Gamma_{\Omega}(\mathbf{p}, \mathbf{p})$ in (26).

For the special case of the rectangle, the boundary approximation (22) can be written

$$\sigma \simeq \frac{4(L_x + L_y)}{\pi k_A L_x L_y} f(\alpha)$$

and figure 3 shows both the result of calculation $f(\alpha)$ in full (for $\alpha > 1$) using (22) and its asymptotic form (as $\alpha \rightarrow \infty$) given in (23). Note also that an evaluation by integration of (26) applies uniformly for all α , including across the critical value $\alpha = 1$, and, except for the negligible corner correction, is completely equivalent to the direct integration of (12) shown in figure 1. In fact evaluation using (50) is significantly faster, involving one integral fewer, although it is restricted to the case of rectangular geometry.

In appendix A, the results obtained here are compared with a modal approach, where a radiation efficiency is calculated for each eigenmode of a rectangular plate. The diffuse field case is then obtained after averaging over many eigenmodes, see figure A2.

5. Conclusion

We have provided asymptotic estimates of acoustic power radiated from vibrating plates whose normal velocity field is homogeneously diffuse, corresponding to ray densities in phase space that are uniform in the corresponding ray-tracing model. Below a critical frequency, where the wavenumber for plate vibration is larger than the acoustic wavenumber, the plate couples weakly to the surrounding air and radiation is driven from the fields near the boundary. We have provided asymptotic estimates of the radiated power in this case in the form of a boundary integral, for both Dirichlet (or simply-supported) and Neumann (or guided) boundary conditions. Surprisingly, radiation is relatively larger in the Dirichlet case even though the velocity amplitude must then vanish on the boundary itself. The results have been validated by comparison to a modal analysis in the separable case of a rectangular plate.

The boundary conditions treated in detail in this paper are rather simple and have been chosen in order to provide a proof-of-principle demonstration of the importance of boundary conditions, so that an analytical treatment using the method of images is possible. The wider conclusion that radiation below a critical frequency can be approximated by a boundary integral will extend to more general and realistic boundary conditions. To treat the more general case, it will be necessary to calculate the boundary corrections to the CF, including for example coupling between propagating and evanescent bending modes, which have significant amplitudes near the boundary. For problems without baffling, it will be necessary to compute also the fields just outside the boundary and to modify the Rayleigh integral (2) accordingly. This is a significantly more complicated calculation, but is, we believe, an entirely tractable one, using the approach for example in [35] to compute boundary corrections.

We have also simplified the analysis by assuming that the diffuse field is uniform except for these boundary corrections, which is equivalent in the analogous ray-tracing model to assuming that the ray density is constant in phase space. A future extension to the case of nonuniform CFs, and a reformulation using Wigner representations in terms of local phase space densities, will be an important addition to turn the approach into a practical tool for sound simulation in engineering contexts.

Acknowledgments

The authors are grateful for the opportunity to contribute to this special edition in the memory of Fritz Haake, whose scientific and pedagogical contributions have contributed enormously to our understanding of the field. The current contribution on the exploitation of ideas from quantum and wave chaos to predict acoustic emission is just a small reflection of this. We also acknowledge the support of Romax Technologies Ltd and Yanmar Co. Ltd. This work has been supported by the European Commission in part by the H2020 RISE-6G Project under Grant 101017011 and in part by the EPSRC under Grant EP/V048937/1.

Data availability statement

All data that support the findings of this study are included within the article (and any supplementary files).

Appendix A. Comparison with a modal approach

We benchmark in this appendix the calculations of radiation efficiency for disordered fields presented in the main text against a more traditional approach based on a modal analysis. This latter approach has the disadvantage of being applicable only to integrable plate geometries, but the rectangular case treated in detail in the main text is such a problem and it is informative to compare the results of these approaches here.

The power radiated by a vibrational eigenmode of the plate, $w_{nm}(x, y)$, denoting the local normal velocity amplitude, is obtained from the following analogue of (25)

$$\Pi'_{nm} = \left(\frac{k_A}{2\pi}\right)^2 \int_D \frac{|W_{nm}(\mathbf{p})|^2}{\sqrt{1-|\mathbf{p}|^2}} d\mathbf{p},$$

where W_{nm} denotes the Fourier transform according to the convention in (24). We also define a corresponding radiation efficiency σ_{nm} , defined in analogy to (5). Each of these modes has a characteristic vibrational wave number k_{nm} , denoted

$$k_{nm} = k_B(\omega_{nm}),$$

where ω_{nm} is the modal frequency and for any frequency ω we define the vibrational wavenumber $k_B(\omega)$ by

$$k_B^2 = \omega \sqrt{\frac{\rho_s h}{B}}, \quad (\text{A.1})$$

where h is the plate thickness, ρ_s is its density,

$$B = \frac{Eh^3}{12(1-\nu^2)}$$

is the bending stiffness, and ν denoted the Poisson ratio. The natural frequencies of the vibrating plate are in both the Dirichlet and Neumann cases given by

$$\omega_{nm} = \sqrt{\frac{B}{\rho_s h} \left[\left(\frac{n\pi}{L_x}\right)^2 + \left(\frac{m\pi}{L_y}\right)^2 \right]}, \quad (\text{A.2})$$

except that the mode numbers are $n, m = 0, 1, 2, \dots$ in the Neumann case and $n, m = 1, 2, \dots$ in the Dirichlet case. We distinguish between k_{nm} and k_B because, if the plate is driven at a nonresonant frequency ($\omega \neq \omega_{nm}$), they are different.

It is instructive to compare the forms of $W_{nm}(\mathbf{p})$ for the two sets of boundary conditions considered, which can be shown to be of the form [10]

$$W_{nm}(\mathbf{p}) = \frac{A_{nm}}{\sqrt{L_x L_y}} \frac{[(-1)^n e^{-ik_A L_x p_x} - 1][(-1)^m e^{-ik_A L_y p_y} - 1]}{\left[\left(\frac{n\pi}{L_x} \right)^2 - k_A^2 p_x^2 \right] \left[\left(\frac{m\pi}{L_y} \right)^2 - k_A^2 p_y^2 \right]} \times \begin{cases} \frac{nm\pi^2}{L_x L_y} & \text{Dirichlet} \\ k_A^2 p_x p_y & \text{Neumann.} \end{cases} \quad (\text{A.3})$$

(Recall that the convention for the Fourier transform in (24) uses the acoustic wavenumber k_A even when dealing with the vibrational problem). Here,

$$A_{nm} = \begin{cases} 1 & \text{for } n = 0 \text{ and } m = 0 \\ \sqrt{2} & \text{for } n = 0 \text{ or } m = 0 \\ 2 & \text{for } n \neq 0 \text{ and } m \neq 0 \end{cases}$$

is a normalisation constant. The relative sizes of the terms in braces are at the root of the relatively greater radiated power for the Dirichlet case when $\alpha > 1$.

Figure A1 shows how a selection of modal efficiencies σ_{nm} vary with frequency by plotting them as a function the parameter

$$\frac{1}{\alpha} = \frac{k_A}{k_{nm}} \propto \omega.$$

It is evident that each of these curves changes considerably from one mode to the next. To make a comparison with the diffuse-field results in the main text, we therefore also calculate averaged efficiencies using

$$\bar{\sigma}_{\text{modal}} = \frac{1}{N^2} \sum_{m=1}^N \sum_{n=1}^N \sigma_{nm}. \quad (\text{A.4})$$

In order to compare this average with the diffuse field result, we note that the latter depends on two wave numbers k_A and k_B (or equivalently k_A , and $\alpha = k_B/k_A$). To distinguish it from the modal average and to emphasise this dual dependence on wave numbers, let us denote it by $\sigma_D(k_A, k_B)$. In this appendix, $\sigma_D(k_A, k_B)$ will be calculated using (50). In order to perform an equivalent average over vibrational wave numbers, we therefore define the corresponding average

$$\bar{\sigma}_{\text{diffuse}}(\alpha) = \frac{1}{N^2} \sum_{m=1}^N \sum_{n=1}^N \sigma_D(k_A = k_{nm}/\alpha, k_B = k_{nm}). \quad (\text{A.5})$$

We compare $\bar{\sigma}_{\text{modal}}$ and $\bar{\sigma}_{\text{diffuse}}$ in figure A2. The results are in good agreement apart from very small values of the radiation efficiency in the Neumann case below $1/\alpha = 0.1$; these deviations are due to insufficient cancellations of relative large terms when truncating the sum (A.4) and are thus of numerical nature. We note that the average of the Dirichlet and Neumann modal

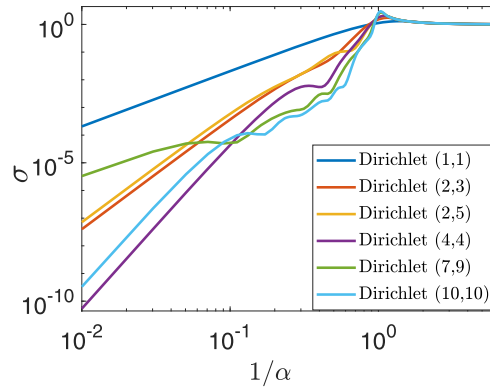


Figure A1. Modal radiation efficiencies σ_{nm} of simply supported plates are shown for a selection of mode numbers (n, m) , which are given in brackets in the legend. There is significant fluctuation from one mode to the next here, which is eliminated in the averaged efficiencies shown in figure A2.

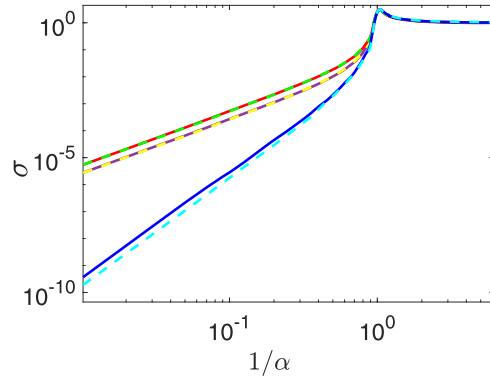


Figure A2. The radiation efficiency of a baffled rectangular plate for different boundary conditions and using both the diffuse-field (solid curves) and modal excitation (dashed curves). Both approaches have been averaged according to (A.5). The diffusive field excitation with Dirichlet (red) and Neumann (blue) boundary conditions as well as the mean value of the radiation efficiency with Dirichlet and Neumann boundary conditions (purple) are compared with the eigenmode excitation for simply supported plates (green), guided plates (cyan), and the mean value (yellow).

results agree well with the diffuse results from the bulk contribution alone, neglecting boundary corrections.

Appendix B. Corner correction in rectangular case

Here, we derive the corner correction $C(\mathbf{p}, \mathbf{p}')$ given in (49) following detailed calculations analogous to those of sections 4.3 and 4.4 for $A(\mathbf{p}, \mathbf{p}')$ and $B(\mathbf{p}, \mathbf{p}')$.

We begin by calculating the Fourier transform of the corner correction (47)

$$\hat{\Gamma}_3(\mathbf{p}, \mathbf{p}') = \int_{\mathbb{R}^2} \int_{\mathbb{R}^2} J_0(\alpha k_A |\mathbf{x} + \mathbf{x}'|) e^{-ik_A \mathbf{p} \cdot \mathbf{x} + ik_A \mathbf{p}' \cdot \mathbf{x}'} d\mathbf{x} d\mathbf{x}'$$

and changing to mean and displacement variables defined in equation (18), according to

$$\begin{aligned} \hat{\Gamma}_3(\bar{\mathbf{p}} - \mathbf{q}/2, \bar{\mathbf{p}} + \mathbf{q}/2) &= \int_{\mathbb{R}^2} \int_{\mathbb{R}^2} J_0(2\alpha k_A |\bar{\mathbf{x}}|) e^{-ik_A \mathbf{q} \cdot \bar{\mathbf{x}} - ik_A \bar{\mathbf{p}} \cdot \mathbf{u}} d\mathbf{u} d\bar{\mathbf{x}} \\ &= \frac{1}{4\pi} \left(\frac{2\pi}{k_A}\right)^4 \delta(\bar{\mathbf{p}}) \delta\left(\left|\frac{\mathbf{q}}{2}\right|^2 - \alpha^2\right). \end{aligned} \tag{B.1}$$

Next, we derive (49) by inserting this into the appropriate analogue of (29) giving

$$\begin{aligned} C(\mathbf{p}, \mathbf{p}') &= \frac{1}{\pi} \int_{\mathbb{R}^2} d\mathbf{p}'' H(\mathbf{p} - \mathbf{p}'') \delta(|\mathbf{p}''|^2 - \alpha^2) H^*(\mathbf{p}' + \mathbf{p}'') \\ &= \langle H(\mathbf{p} - \mathbf{p}_\alpha) H^*(\mathbf{p}' + \mathbf{p}_\alpha) \rangle, \end{aligned}$$

where the average is over the direction of \mathbf{p}_α as in the calculations of $A(\mathbf{p}, \mathbf{p}')$ and $B(\mathbf{p}, \mathbf{p}')$ in the main text.

Substituting the defining equation for $H(\mathbf{p})$, noting that we require only the diagonal components with $\mathbf{p} = \mathbf{p}'$ and letting Ω be the first quadrant $0 < x, x', y, y' < \infty$, leads to

$$\begin{aligned} C(\mathbf{p}, \mathbf{p}) &= \left\langle \int_{\Omega} \int_{\Omega} e^{-ik_A(\mathbf{p} - \mathbf{p}_\alpha) \cdot \mathbf{x} + ik_A(\mathbf{p} + \mathbf{p}_\alpha) \cdot \mathbf{x}'} d\mathbf{x} d\mathbf{x}' \right\rangle \\ &= \left\langle \frac{1}{ik_A(p_x - \alpha \cos \theta - i0^+)} \times \frac{1}{ik_A(p_y - \alpha \sin \theta - i0^+)} \right. \\ &\quad \left. \times \frac{1}{-ik_A(p_x + \alpha \cos \theta + i0^+)} \times \frac{1}{-ik_A(p_y - \alpha \sin \theta + i0^+)} \right\rangle \\ &= \frac{1}{k_A^4} \left\langle \frac{1}{p_x^2 - (\alpha \cos \theta + i0^+)^2} \times \frac{1}{p_y^2 - (\alpha \sin \theta + i0^+)^2} \right\rangle. \end{aligned}$$

When $\alpha > 1$, then for each \mathbf{p} inside the unit disk D we find that there are eight poles along the integration path over θ corresponding to the average $\langle \cdot \rangle$, 4 from each of the two factors in the denominator. Evaluating the integral using residue calculus, we find that 2 of the 4 poles for each of the factors do not contribute and the remaining poles cancel pairwise, so that

$$C(\mathbf{p}, \mathbf{p}) = 0$$

when evaluated for the special case of a quadrant [27]. Therefore the corner contribution to the asymptotic development of the boundary integral vanishes in the special case of a right angle and Dirichlet or Neumann boundary conditions, as claimed in the main text. Note however, that the underlying destructive cancellation of the corner correction is incomplete when spatial integration is restricted to the true finite domain Ω rather than being extended to the whole

quadrant. Therefore, for example, the corner contribution to the rectangle geometry in (50) does not exactly vanish, although it is numerically insignificant in our calculations.

Appendix C. Large α asymptotics

We here justify the asymptotic (as $\alpha \rightarrow \infty$) forms given in (23) for the function $f(\alpha)$ defined in (22). In this limit $f(\alpha)$ becomes

$$f(\alpha) \simeq \frac{1}{2\pi} \int_0^{2\pi} d\phi \int_0^1 dp \frac{p}{\alpha\sqrt{1-p^2}} \begin{cases} \frac{1}{\alpha^2} & \text{Dirichlet,} \\ \frac{p^2 \sin^2 \phi}{\alpha^4} & \text{Neumann,} \end{cases}$$

$$= \int_0^1 dp \frac{p}{\alpha^5\sqrt{1-p^2}} \begin{cases} \alpha^2 & \text{Dirichlet,} \\ \frac{1}{2}p^2 & \text{Neumann.} \end{cases}$$

Making use of the integrals

$$\int_0^1 \frac{p}{\sqrt{1-p^2}} dp = 1, \quad \text{and} \quad \int_0^1 \frac{p^3}{\sqrt{1-p^2}} dp = \frac{2}{3},$$

this then reduces to (23), as claimed.

ORCID iDs

Neekar M Mohammed  <https://orcid.org/0000-0003-0878-8210>
 Stephen C Creagh  <https://orcid.org/0000-0002-6584-8614>
 Gregor Tanner  <https://orcid.org/0000-0001-5756-274X>

References

- [1] Tanner G 2009 *J. Sound Vib.* **320** 1023–38
- [2] Fahy F and Gardonio P 2007 *Sound and Structural Vibration: Radiation, Transmission and Response EngineeringPro Collection* (Amsterdam: Elsevier)
- [3] Kac M 1966 *Am. Math. Mon.* **73** 1–23
- [4] Balian R and Bloch C 1970 *Ann. Phys., NY* **60** 401–47
- [5] Baltes H and Hilf E 1976 *Spectra of Finite Systems* (Mannheim/Wien/Zurich: Bibliographisches Institut—Wissenschaftsverlag)
- [6] Junger M and Feit D 1986 *Sound, Structures, and Their Interaction* (Cambridge, MA: MIT Press)
- [7] Cremer L, Heckl M and Ungar E 1973 *Structure-borne Sound; Structural Vibrations and Sound Radiation at Audio Frequencies* (Berlin: Springer)
- [8] Maidanik G 1962 *J. Acoust. Soc. Am.* **34** 809–26
- [9] Wallace C E 1972 *J. Acoust. Soc. Am.* **51** 936–45
- [10] Wallace C E 1972 *J. Acoust. Soc. Am.* **51** 946–52
- [11] Gomperts M 1974 *Acta Acust.* **30** 320–27
- [12] Heckl M 1977 *Acta Acust.* **37** 155–66
- [13] Leppington F G, Broadbent E G and Heron K H 1982 *Proc. R. Soc. A* **382** 245–71

- [14] Williams E G 1983 *J. Acoust. Soc. Am.* **73** 1520–4
- [15] Delande D and Sornette D 1997 *J. Acoust. Soc. Am.* **101** 1793–807
- [16] Maidanik G 1963 *J. Acoust. Soc. Am.* **35** 115
- [17] Leppington F, Broadbent E G and Heron K 1984 *Proc. R. Soc. A* **393** 67–84
- [18] Gomperts M 1977 *Acta Acust.* **37** 93–102
- [19] Berry A, Guyader J L and Nicolas J 1990 *J. Acoust. Soc. Am.* **88** 2792–802
- [20] Yoo J W 2010 *J. Mech. Sci. Technol.* **24** 1111–8
- [21] Creagh S C, Gradoni G, Hartmann T and Tanner G 2016 *J. Phys. A: Math. Theor.* **50** 045101
- [22] Berry M V 1977 *J. Phys. A: Math. Gen.* **10** 2083
- [23] Gradoni G, Yeh J-H, Xiao B, Antonsen T M, Anlage S M and Ott E 2014 *Wave Motion* **51** 606–21
- [24] Hemmady S, Antonsen T M, Ott E and Anlage S M 2012 *IEEE Trans. Electromagn. Compat.* **54** 758–71
- [25] Tanner G and Søndergaard N 2007 *J. Phys. A: Math. Theor.* **40** R443
- [26] Hartmann T, Morita S, Tanner G and Chappell D J 2019 *Wave Motion* **87** 132–50
- [27] Mohammed N M 2021 *Vibroacoustics of complex structures—a wave chaos approach PhD Thesis* The University of Nottingham
- [28] Rayleigh L 1897 *London, Edinburgh Dublin Phil. Mag. J. Sci.* **43** 259–72
- [29] Williams E G 1999 *Fourier Acoustics: Sound Radiation and Nearfield Acoustical Holography* (Amsterdam: Elsevier)
- [30] Snyder S D and Tanaka N 1995 *J. Acoust. Soc. Am.* **97** 1702–9
- [31] Morse P M and Bolt R H 1944 *Rev. Mod. Phys.* **16** 69
- [32] Schroeder M R 1959 *J. Acoust. Soc. Am.* **31** 1407–14
- [33] Schroeder M R 1962 *J. Acoust. Soc. Am.* **34** 1819–23
- [34] Lyon R H 1969 *J. Acoust. Soc. Am.* **45** 545–65
- [35] Berry M V 2002 *J. Phys. A: Math. Gen.* **35** 3025
- [36] Norton M and Karczub D 2003 *Fundamentals of Noise and Vibration Analysis for Engineers* (Cambridge: Cambridge University Press)
- [37] Gradshteyn I S and Ryzhik I M 2014 *Table of Integrals, Series, and Products* (New York: Academic)
- [38] Korenev B 2002 *Bessel Functions and Their Applications Analytical Methods and Special Functions* (Boca Raton, FL: CRC Press)